

# MicroMIL: Graph-based Contextual Multiple Instance Learning for Patient Diagnosis Using Microscopy Images

JongWoo Kim<sup>1\*</sup>Bryan Wong<sup>1\*</sup>YoungSin Ko<sup>2</sup>MunYong Yi<sup>1†</sup><sup>1</sup>KAIST and <sup>2</sup>Seegene Medical Foundation<sup>1</sup>{gsds4885, bryan.wong, munyi}@kaist.ac.kr, <sup>2</sup>noteasy@mf.seegene.com

## Abstract

Current histopathology research has primarily focused on using whole-slide images (WSIs) produced by scanners with weakly-supervised multiple instance learning (MIL). However, WSIs are costly, memory-intensive, and require extensive analysis time. As an alternative, microscopy-based analysis offers cost and memory efficiency, though microscopy images face issues with unknown absolute positions and redundant images due to multiple captures from the subjective perspectives of pathologists. To this end, we introduce MicroMIL, a weakly-supervised MIL framework specifically built to address these challenges by dynamically clustering images using deep cluster embedding (DCE) and Gumbel Softmax for representative image extraction. Graph edges are then constructed from the upper triangular similarity matrix, with nodes connected to their most similar neighbors, and a graph neural network (GNN) is utilized to capture local and diverse areas of contextual information. Unlike existing graph-based MIL methods designed for WSIs that require absolute positions, MicroMIL efficiently handles the graph edges without this need. Extensive evaluations on real-world colon cancer (Seegene) and public BreakHis datasets demonstrate that MicroMIL outperforms state-of-the-art (SOTA) methods, offering a robust and efficient solution for patient diagnosis using microscopy images. The code is available at <https://anonymous.4open.science/r/MicroMIL-6C7C>

## 1. Introduction

Cancer remains a significant global health challenge, prompting extensive research in various fields including medical informatics [38]. Timely detection is crucial for improving survival rates, yet conventional cancer diagnosis conducted by pathologists suffers from subjectivity, bias, and high manual labor costs [2, 4, 7, 15]. To address these

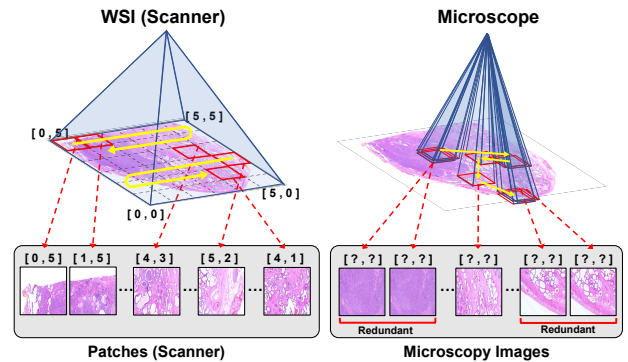


Figure 1. **Left:** Valid patches from WSI (scanner) are acquired through a window-sliding approach and have absolute positions. **Right:** Microscopy images lack known positions and have many redundancies due to the subjective capture by pathologists.

challenges, advancements in deep learning and tissue digital scanners have facilitated the development and analysis of whole-slide images (WSIs), enhancing diagnostic accuracy and efficiency.

While WSIs provide detailed views of human tissue structures and disease-related anomalies, their typical composition of billions of pixels makes direct training of deep neural networks impractical. Consequently, the prevailing methods follow a patch-based paradigm [9, 27]. To handle the large number of patches and alleviate the workload on pathologists from labeling each patch, weakly-supervised multiple instance learning (MIL) has emerged as a viable solution, requiring only WSI-level labels without fine-grained (patch-level) annotations [12].

In histopathology, understanding tissue context through patterns is crucial [28, 34, 42], yet existing MIL models [20, 35, 44] struggle to analyze this effectively using only individual patches. Graph-based MIL approaches address this by modeling the relationships between patches, enabling a more comprehensive understanding of tissue anomalies and their spatial context. Models such as WSI-HGNN [8] and H2-MIL [18] enhance the exchange of contextual infor-

\*Equal contribution

†Corresponding author

mation across regions by considering relationships among multi-resolution patches. Additionally, GDS-MIL [5] introduces a novel approach by integrating graph attention layers (GAT) to infuse spatial contextual information into MIL models, further improving the accuracy and robustness of cancer detection.

Recently, microscopy-based analysis has gained attention for its cost and memory efficiency compared to WSIs produced by scanners [1, 10, 14, 15, 21, 26, 36]. Despite these advances, capturing contextual information in microscope images remains a critical challenge. Existing graph-based MIL models designed for WSIs [5, 8, 18] require **absolute** positions to construct graph edges, which are not available in microscope datasets. As shown in Figure 1 (Left), tiling patches from WSIs using a scanner follows a window-sliding approach, allowing access to absolute positions. In contrast, Figure 1 (Right) illustrates that microscopy images are acquired from the subjective perspective of pathologists, resulting in unknown absolute positions and redundant patches due to multiple captures. This lack of absolute positions hinders the use of existing graph-based MIL models, preventing effective analysis of relationships between microscope images within a patient. Moreover, redundancy in images is problematic because creating edges based on similarity significantly increases connections between duplicate images, reducing connectivity with images from diverse areas. This could slow down overall information exchange and ultimately hampers contextual understanding.

Given the unique characteristics of microscopy images, such as unknown absolute positions that hinder graph edge construction and the presence of redundant images, we propose a weakly-supervised MIL framework to alleviate the workload of pathologists. Our approach extracts representative images and incorporates their relative positions to capture contextual information, thereby improving the prediction of patient diagnoses. To this end, we introduce Graph-based Multiple Instance Learning for Patient Diagnosis Using **Microscopy Images (MicroMIL)**. Specifically, we dynamically cluster microscopy images using deep cluster embedding (DCE) [19] and employ Gumbel Softmax [22] to extract a representative image from each cluster. Subsequently, we utilize graph neural networks (GNNs) to connect representative images based on their similarity and model the relationships between images. By integrating local contextual information within clusters and combining it with contextual information between clusters, MicroMIL effectively captures and leverages the spatial and contextual relationships present in microscopy images.

We extensively evaluate our method on two microscopy datasets: a real-world colon cancer dataset (Seegene), which contains a larger number of microscopy images and exhibits a more severe redundancy issue compared to the public dataset, and the public BreakHis dataset [4] for breast

cancer. Our method outperforms various state-of-the-art (SOTA) methods used for WSI scanners, thanks to the DCE that effectively addresses the redundancy issue and the GNNs that extract contextual information based on representative image similarity. Our results demonstrate that MicroMIL provides a robust and efficient solution for patient diagnosis using microscopy images, overcoming key limitations of existing methods designed for scanner-derived WSIs.

## 2. Related Work

### 2.1. MIL for WSIs (Scanner)

Weakly-supervised MIL has significantly impacted the histopathology field by utilizing WSI labels without requiring individual patch annotations. Initial methods used Mean or Max Pooling for feature aggregation, but these have evolved into more sophisticated techniques. ABMIL [20] calculates attention scores for each patch to enhance the aggregation process. Building on this, MSDAMIL [17] combines multiple-instance, domain adversarial, and multi-scale learning frameworks to improve robustness. DSMIL [29] further refines MIL models with self-supervised contrastive learning and proposes considering the distance between each patch and the critical patch. Transformer-based approaches like TransMIL [35] and attention modules in MIMIL [24] have effectively captured patch relationships. DTFD-MIL [44] leverages Grad-CAM [33] to derive patch probabilities, offering more precise predictions and better interpretability. A recent method, HAGMIL [41], incorporates multiple resolutions of the WSIs to further improve analysis.

Graph-based MIL methods have recently been proposed to extract contextual information between patches. WSI-HGNN [8] and H2-MIL [18] actively model the exchange and integration of contextual information across regions by considering the relationships among multi-resolution patches. GDS-MIL [5] proposes a novel approach by integrating graph attention layers (GAT) to infuse spatial contextual information into MIL models. While these methods effectively address the unique characteristics of WSIs, they do not account for the specific characteristics of microscopy images: unknown absolute positions (making graph-based MIL models designed for WSIs inapplicable) and redundant images.

### 2.2. Patient Diagnosis Using Microscopy Images

Previous research often relies on simple statistical techniques for patient-level diagnosis. Nguyen *et al.* [31] employ ensemble methods for colorectal tissue image classification, utilizing soft voting on VGG16 and CapsNet outcomes. Gandomkar *et al.* [13] propose an ensemble approach using meta-decision trees (MDT) for patient clas-

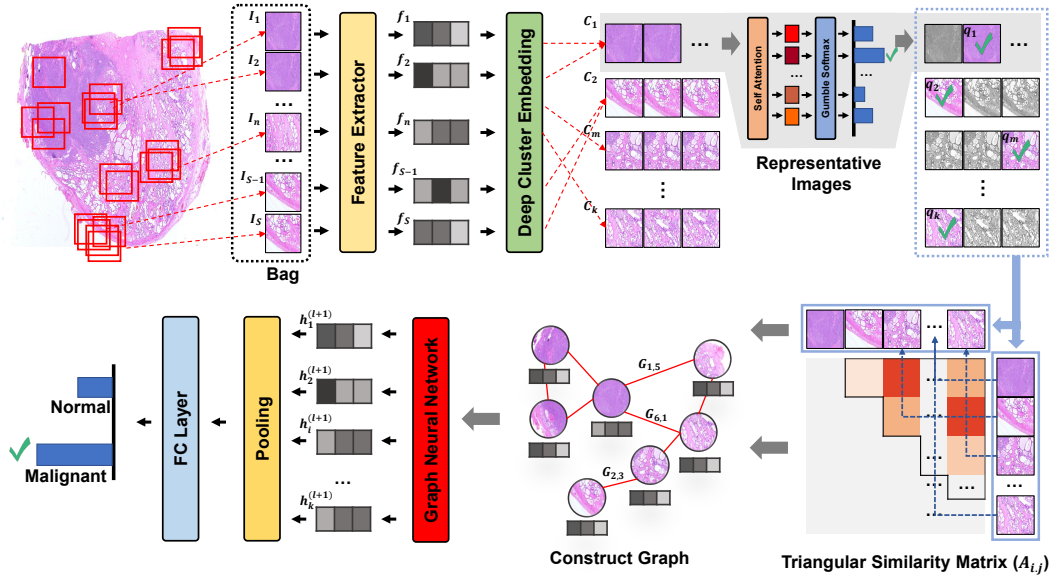


Figure 2. The proposed end-to-end MicroMIL framework processes patient microscopy images using a pre-trained feature extractor and deep cluster embedding (DCE) to eliminate redundancy and select representative images with Gumbel Softmax. Graph edges are then constructed from the upper triangular similarity matrix, connecting nodes to their most similar neighbors via Gumbel Softmax. The graph neural network (GNN) then captures local and diverse areas of contextual information based on representative image similarity.

Dataset	VGH [3]	MHIST [39]	Kowal [25]	Filipcuk [11]	BreakHis [4]	Seegene
Average Redundant Images	1.2	9.6	10	11	96.4	150.27

Table 1. Comparison of the average number of redundant images across various public datasets and a real-world dataset (Seegene). The real-world dataset shows a substantially higher number of redundant images.

sification while Han *et al.* [16] leverage GoogleNet and majority voting for breast tissue histopathology image classification.

MIL has also been applied to microscopy images. Pal *et al.* [32] utilize sparse attention for instance aggregation in a deep MIL framework to analyze cervical histopathological images more cost-effectively using microscopy images. Recently, Yang *et al.* [43] introduce the hierarchical aggregation network for MIL, evaluating its performance on protein subcellular localization using immunofluorescence images and gene annotation with spatial gene expression images.

Despite these advancements, existing studies often rely on simple machine learning and statistical methods, which exhibit limitations in both accuracy and efficiency. Furthermore, current MIL models are not specifically designed to address the unique characteristics of H&E microscopy images. Our study emphasizes the importance of eliminating redundant images and considering the contextual information between representative images to achieve accurate patient-level predictions.

### 2.3. Microscope Datasets

In the field of microscopy image analysis, several benchmark datasets are commonly used for research. The ICIAR2018 dataset<sup>1</sup> contains 1376 breast cancer samples at magnifications from x20 to x200. Additionally, datasets from the Netherlands Cancer Institute (NKI) and Vancouver General Hospital (VGH) offer 248 and 328 breast cancer samples at x200 magnification [3]. These datasets are complemented by others like BreakHist [4] for breast cancer and MHIST [39] for various cancers.

While these research-focused datasets are invaluable, they offer differ significantly from real-world clinical data, which typically includes more redundant images per patient (Table 1). Benchmark public datasets are curated to remove unnecessary data, which is not reflective of the complexity, encountered in clinical settings. To enhance the practicality and robustness of our approach, we utilize a real-world microscopy dataset from the Seegene Medical Foundation (details available in the **Supplementary Information**) and the public BreakHis dataset [4] for breast cancer. This study aims to predict patient diagnoses using microscope images,

<sup>1</sup><https://iciar2018-challenge.grand-challenge.org/Dataset/>

relying solely on patient labels without image-level annotations.

### 3. Proposed Method

We present MicroMIL, a weakly-supervised MIL framework adapted to the unique characteristics of microscopy images (Figure 2). It consists of three main components: 1) extracting features using a pre-trained feature extractor model, 2) removing redundancy through deep cluster embedding (DCE) and then extracting representative images with Gumbel Softmax, and 3) constructing a graph neural network (GNN) based on representative patch similarity to capture both local (within-cluster) and regional (between-cluster) contextual information. The details of the process can be found in Algorithm 1.

---

#### Algorithm 1 MicroMIL

---

- 1: **Input:** Set of images from patient  $I_s$
  - 2: **Output:** Predicted diagnosis  $\hat{y}^{(p)}$
  - 3: Extract features  $F_p = \{f_s^{(p)} = E(I_s^{(p)}) \mid I_s^{(p)} \in I_p\}$
  - 4: Initialize cluster centroids  $\mu_k^{(p)}$
  - 5: **repeat**
  - 6:   Assign  $f_i^{(p)}$  to nearest centroid  $\mu_k^{(p)}$
  - 7:   Update centroids  $\mu_k^{(p)}$
  - 8: **until** convergence
  - 9: **for** each cluster  $k$  **do**
  - 10:   Compute weights  $t_k^{(p)}$ , attention weights  $\alpha_{k,i}^{(p)}$  using Gumbel Softmax
  - 11:   Compute representative feature  $q_k^{(p)}$
  - 12: **end for**
  - 13: Compute similarity triangular matrix  $A_{i,j}^{(p)}$
  - 14: Construct graph  $\mathcal{G}^{(p)} = (\mathcal{V}^{(p)}, \mathcal{E}^{(p)})$  using  $\mathcal{E}_{i,j}^{(p)} = 1$  if  $A_{i,j}^{(p)} = \max(\sigma(A_{k,j}^{(p)}))$ , otherwise  $\mathcal{E}_{i,j}^{(p)} = 0$
  - 15: **for** each layer  $l$  **do**
  - 16:   **for** each node  $i$  in  $\mathcal{V}^{(p)}$  **do**
  - 17:     Aggregate features  $h_i^{(l+1)(p)}$
  - 18:   **end for**
  - 19: **end for**
  - 20: Compute WSI representation  $\bar{h}^{(p)}$  as the mean of  $h_i^{(L)(p)}$
  - 21: Compute predicted diagnosis  $\hat{y}^{(p)} = \text{MLP}(\bar{h}^{(p)})$
  - 22: **return**  $\hat{y}^{(p)}$
- 

#### 3.1. Feature Extractor

MIL can be categorized into two types: instance-based and embedding-based MIL [12]. Embedding-based MIL, which provides richer representation, has become the preferred research focus due to its effectiveness in classifying WSIs [6]. Following the common practice in embedding-based MIL, we extract microscopy images  $I_s$  using a pre-

trained feature extractor  $E$  (Equation 1) where  $S_p$  represents the number of images in patient  $p$ .

$$f_s^{(p)} = E(I_s^{(p)}), \quad s \in \{1, \dots, S_p\} \quad (1)$$

#### 3.2. Deep Cluster Embedding

We utilize deep cluster embedding (DCE) [40] as a key component of our methodology to remove redundant images, which occur frequently in microscope datasets, as shown in Table 1.

Let  $F_p = \{f_1^{(p)}, f_2^{(p)}, \dots, f_{S_p}^{(p)}\}$  denote the set of features for patient  $p$  obtained from the feature extraction process. Additionally, let  $C_p = \{c_1^{(p)}, c_2^{(p)}, \dots, c_K^{(p)}\}$  be the set of image cluster assignments for patient  $p$ , where  $K$  denotes the number of clusters.

The deep cluster function can be formulated as follows:

$$DCE(F_p) = \min_C \sum_{i=1}^{S_p} \sum_{k=1}^K \|f_i^{(p)} - \mu_k^{(p)}\|^2 \cdot \alpha(c_i^{(p)} = k) \quad (2)$$

Here,  $\mu_k^{(p)}$  represents the centroid of cluster  $k$  and  $\alpha$  is the indicator function that equals 1 if the condition inside the parentheses is true and 0 otherwise.

The deep cluster function aims to minimize the distances between data points and their respective cluster centroids while simultaneously updating the cluster assignments to ensure compact and well-separated clusters in the feature space. This process iteratively refines the embeddings and cluster assignments until convergence, resulting in meaningful representations of the data that are suitable for subsequent classification tasks.

#### 3.3. Representative Images

Through the aforementioned method, we perform image clustering to understand the relationships between images within the same area. To eliminate redundancy, we then select the most significant image within each area. This process reduces interactions within the same area (cluster) while facilitating information exchange between different areas (between clusters). Initially, we use Equation 3 to calculate the weights between images within the clusters. Subsequently, we employ the Gumbel Softmax [22], which enables backpropagation to select the most influential representative image.

The weight  $t_k^{(p)}$  for cluster  $k$  of patient  $p$  is calculated as follows:

$$t_k^{(p)} = W_1 \cdot (DCE(F^{(p)})_k \cdot F^{(p)}), \quad k \in \{1, 2, \dots, K\} \quad (3)$$

where  $W_1$  denotes the weight of self-attention, where  $W_1 \in \mathbb{R}^{d \times 1}$ ,  $DCE(F^{(p)})_k$  represents the features of cluster  $k$ , and  $F^{(p)}$  is the set of features for patient  $p$ .

The Gumbel Softmax function is then used to calculate the attention weight  $\alpha_k, i^{(p)}$  for each image  $i$  in cluster  $k$  of patient  $p$ :

$$\alpha_{k,i}^{(p)} = \frac{\exp\left(\frac{t_{k,i}^{(p)} + g_i}{\tau}\right)}{\sum_{j=1}^{N_k^{(p)}} \exp\left(\frac{t_{k,j}^{(p)} + g_j}{\tau}\right)} \quad (4)$$

where  $g_i$  is the noise sampled from a Gumbel distribution and  $\tau$  is the temperature parameter.

The representative feature  $q_k^{(p)}$  for cluster  $k$  of patient  $p$  is then computed as follows:

$$q_k^{(p)} = \sum_{i=1}^{N_k^{(p)}} \alpha_{k,i}^{(p)} \cdot (DCE(F^{(p)})_k \cdot F^{(p)}) \quad (5)$$

Let  $Q^{(p)} = \{q_1^{(p)}, q_2^{(p)}, \dots, q_K^{(p)}\}$  represent the set of representative features of patient  $p$  in cluster  $k$ , where  $K$  denotes the total number of clusters.  $N_k^{(w)}$  is the number of patches included in the  $k$ -th cluster of patient  $p$

### 3.4. Graph-based Aggregation

Patches derived from WSI via scanners have defined absolute positions, facilitating the identification of neighboring patches. However, microscopy images lack these absolute coordinates, complicating the task of neighbor identification. To address this challenge, we determine the neighbors of representative images through relative positioning and maximize interactions using graph-based aggregation.

#### 3.4.1 Constructing Graph

The graph is constructed by defining similarities between representative images, represented as nodes. The similarity in Equation 6 computes a similarity matrix  $A_{i,j}^{(p)}$  based on image features. To form the graph, we use the upper triangular part of the similarity matrix, ensuring that each node connects to its most similar neighbors using the Gumbel Softmax function.

$$A_{i,j}^{(p)} = \text{similarity}(q_i^{(p)}, q_j^{(p)}) \quad (6)$$

Here,  $A_{i,j}^{(p)}$  denotes the similarity between image features  $q_i^{(w)}$  and  $q_j^{(w)}$  for patient  $p$ . To construct the graph  $\mathcal{G}^{(p)}$ , we create an edge matrix  $\mathcal{E}^{(p)}$  using the upper triangular part of  $A^{(p)}$  and the Gumbel Softmax function, as defined in Equation 7.

$$\mathcal{E}_{i,j}^{(p)} = \begin{cases} 1, & \text{if } A_{i,j}^{(p)} = \max_{k \in \mathcal{N}(i)} (\sigma(A_{k,j}^{(p)})), \\ 0, & \text{otherwise} \end{cases} \quad (7)$$

$\mathcal{E}_{i,j}^{(p)}$  represents the presence (1) or absence (0) of an edge between node  $i$  and node  $j$  in the graph for patient  $p$ , with  $i < j$  ensuring that only the upper triangular part is considered. The function  $\sigma$  is the Gumbel Softmax function.

The graph  $\mathcal{G}^{(p)}$  is then formed by connecting nodes based on the edge matrix  $\mathcal{E}^{(p)}$ :

$$\mathcal{G}^{(p)} = (\mathcal{V}^{(p)}, \mathcal{E}^{(p)}) \quad (8)$$

where  $\mathcal{V}^{(p)}$  is the set of nodes representing the representative images ( $\mathcal{V}^{(p)} = Q^{(p)}$ ), and  $\mathcal{E}^{(p)}$  is the set of edges as defined by the edge matrix  $\mathcal{E}^{(p)}$ .

#### 3.4.2 Graph Neural Network

In the graph  $\mathcal{G}^{(p)}$ , nodes represent representative images and edges represent their relationships. The graph attention network (GAT) effectively models interactions between nodes by assigning different weights to adjacent nodes. This can be expressed as follows:

$$h_i^{(l+1)(p)} = \sigma \left( \sum_{j \in \mathcal{N}(i)} \alpha_{i,j}^{(l)(p)} W^{(l)} h_j^{(l)(p)} \right) \quad (9)$$

$h_i^{(l)(p)}$  is the feature representation of node  $i$  for patient  $p$  at layer  $l$ . The set  $\mathcal{N}(i)$  represents the adjacent nodes to node  $i$  in graph  $\mathcal{G}^{(p)}$  while  $\alpha_{i,j}^{(l)(p)}$  indicates the attention coefficient between nodes  $i$  and  $j$  at layer  $l$  for patient  $p$ . The matrix  $W^{(l)}$  is the weight matrix at layer  $l$  and  $\sigma$  denotes the activation function, such as ReLU [30, 37].

The attention coefficients  $\alpha_{i,j}^{(l)(p)}$  are computed as follows:

$$\alpha_{i,j}^{(l)(p)} = \frac{\exp \left( \sigma \left( a^{(l)T} \left[ W^{(l)} h_i^{(l)(p)} \parallel W^{(l)} h_j^{(l)(p)} \right] \right) \right)}{\sum_{k \in \mathcal{N}(i)} \exp \left( \sigma \left( a^{(l)T} \left[ W^{(l)} h_i^{(l)(p)} \parallel W^{(l)} h_k^{(l)(p)} \right] \right) \right)} \quad (10)$$

Here,  $a^{(l)}$  is a learnable weight vector at layer  $l$ ,  $[\cdot \parallel \cdot]$  denotes concatenation, and  $\sigma$  represents the Leaky ReLU activation function.

The representations of nodes are aggregated to obtain a WSI representation  $\bar{h}^{(p)}$  by averaging all node representations:

$$\bar{h}^{(p)} = \frac{1}{|\mathcal{V}^{(p)}|} \sum_{i \in \mathcal{V}^{(p)}} h_i^{(L)(p)} \quad (11)$$

This aggregated representation is then fed into a multi-layer perceptron (MLP) to predict the target variable  $y^{(p)}$ :

$$\hat{y}^{(p)} = \text{MLP}(\bar{h}^{(p)}) \quad (12)$$

Where  $\hat{y}^{(p)}$  is the predicted value of the target variable for patient  $p$ .

### 3.5. Training and Optimization

The entire framework, including the feature extractor, clustering, representative image extraction, and GNN is trained end-to-end. The loss function used for optimization is the cross-entropy loss, defined as follows:

$$\mathcal{L} = -\frac{1}{P} \sum_{p=1}^P \left[ y^{(p)} \log(\hat{y}^{(p)}) + (1 - y^{(p)}) \log(1 - \hat{y}^{(p)}) \right] \quad (13)$$

$P$  is the total number of patients in the training set,  $y^{(p)}$  is the ground-truth label for patient  $p$ , and  $\hat{y}^{(p)}$  is the predicted probability for patient  $p$ .

## 4. Experiments

### 4.1. Datasets

Prior studies have primarily used datasets collected in controlled environments as benchmark datasets. However, real-world microscopic datasets contain significantly more images (Table 2) and exhibit a higher number of redundant images (Table 1). To demonstrate the practicality and robustness of our approach, we utilize a real-world microscope dataset for colon cancer from the Seegene Medical Foundation (details available in the **Supplementary Information**) and the public BreakHis dataset [4] for breast cancer. The goal of this study is to predict patient diagnosis based on microscope images for each patient. It is important to note that only patient labels are used for both datasets, without image-level labels.

	Seegene		BreakHis	
	# Images	# Patients	# Images	# Patients
Malignant	82,761	406	5,429	57
Normal	52,339	493	2,480	24

Table 2. Comparison of the number of images and patients in Seegene and BreakHis datasets.

### 4.2. Baselines

We compared MicroMIL against SOTA MIL models used for WSI from scanners [17, 20, 29, 35, 44] in the weakly-supervised setting (only patient labels are used). Additional details regarding the baselines can be found in the **Supplementary Information**. The reported result of DTFD-MIL is based on the AFS variant. Importantly, direct comparison with existing graph-based MIL models [5, 8, 18] is not feasible because these models require absolute positional information to construct graph edges, which is not available in the microscope datasets.

### 4.3. Implementation Details

To ensure fair comparison, we used ResNet18 pre-trained on ImageNet as the feature extractor for both MicroMIL and the baselines. We set the hidden dimension across all MIL models to 128 to maintain fairness. For other hyperparameters, we followed the default settings from the original papers to achieve their best performance across all datasets. For MicroMIL, we experimented with a dropout rate of 0.5 and learning rates within the range of  $\{1, 3, 5\} \times 10^{-3}$ . We utilized the Adam optimizer [23] for model optimization and applied an early stopping mechanism with a patience of 5 epochs. The implementations were made using the PyTorch framework and trained on an NVIDIA GeForce RTX 3080 GPU.

### 4.4. Metrics

We evaluated the performance using three metrics: Macro-F1, Micro-F1, and area under the curve (AUC). The Macro-F1 score balances precision and recall, making it suitable for imbalanced datasets. Micro-F1 measures overall classification correctness, though it may be affected by class imbalances. AUC assesses the model’s ability to distinguish between positive and negative cases, with higher values indicating better discrimination.

## 5. Results

The primary goal of these experiments is to address the following research questions:

- RQ1: Does the proposed MIL method outperform existing SOTA MIL models used for WSI from scanners?
- RQ2: Do the extracted representative images in diverse areas enhance contextual information?
- RQ3: Does connecting each node to its most similar neighbors during edge generation in GNN enhance contextual information?

### 5.1. Baselines Comparison (RQ1)

Table 3 shows that MicroMIL consistently surpasses baseline MIL models across all evaluated metrics on both real-world and public datasets. This performance advantage stems from MicroMIL’s specific design to address two key characteristics of microscope datasets: image redundancy and missing absolute positions. In contrast, existing MIL models are designed for WSIs obtained from scanners, which do not account for these characteristics. By effectively tackling the unique characteristics present, MicroMIL proves to be exceptionally well-suited for patient diagnosis using microscopy images.

Model	Seegene			BreakHis		
	Macro-F1	Micro-F1	AUC	Macro-F1	Micro-F1	AUC
ABMIL [ICML'18] [20]	0.9650	0.9650	0.9913	0.8805	0.8929	0.8947
MS-DA-MIL [CVPR'20] [17]	0.9781	0.9767	0.9964	<u>0.9268</u>	0.8929	0.9591
DSMIL [CVPR'21] [29]	0.9844	<u>0.9844</u>	0.9984	0.8155	0.8214	0.8947
TransMIL [NeurIPS'21] [35]	0.9805	0.9805	0.9922	<u>0.9268</u>	0.8929	<u>0.9825</u>
DTFD-MIL [CVPR'22] [44]	0.9850	<u>0.9844</u>	0.9988	<u>0.9222</u>	<u>0.9286</u>	<u>0.9766</u>
<b>MicroMIL (Ours)</b>	<b>0.9925</b>	<b>0.9922</b>	<b>0.9994</b>	<b>0.9730</b>	<b>0.9643</b>	<b>0.9942</b>

Table 3. Performance metrics of baselines and the proposed MicroMIL on the Seegene and BreakHis datasets, with the best results are highlighted in **bold** and the second-best results are underlined.

Metric	# of Cluster K									
	1	2	3	4	5	6	7	8	9	10
<b>Macro-F1</b>	<b>0.993</b>	0.988	0.973	0.961	0.953	0.965	0.973	0.950	0.927	0.930
<b>Micro-F1</b>	<b>0.992</b>	0.986	0.971	0.961	0.953	0.965	0.973	0.950	0.934	0.933
<b>AUC</b>	<b>0.999</b>	0.999	0.998	0.996	0.992	0.996	0.997	0.992	0.987	0.987

Table 4. Impact of an increased number of clusters on the effect of contextual information in the Seegene dataset.

## 5.2. Representative Images in Diverse Areas (RQ2)

To validate the hypothesis that extracting representative images from diverse areas enhances contextual information, we employ K-means clustering to extract all images in one patient based on the number of clusters. Figure 3 illustrates that when  $K = 1$  (all data points are assigned to a single cluster), the connections (red line) based on the maximum similarity are between images in diverse areas. However, as  $K$  increases, the connectivity becomes overly localized. The trend is further shown in Table 4 which the highest performance of the evaluated metrics is achieved when  $K = 1$ . Following this observation, it is crucial to extract representative images from diverse areas to obtain more effective contextual information.

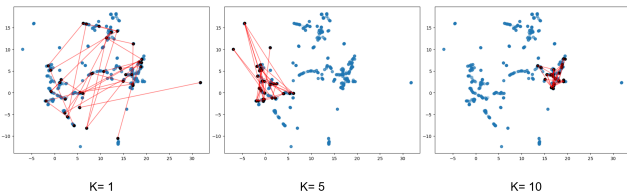


Figure 3. Visualization of image node connectivity variation across clusters, with the red line indicating maximum similarity between image nodes. Higher  $K$  values result in overly localized connectivity, indicating preference for  $K = 1$  to emphasize connection to diverse areas.

## 5.3. Similarity-based Edges in GNN (RQ3)

Contrary to WSIs, where absolute positions are available, microscopy images lack this spatial information, posing a challenge for creating edges. To address this, we introduce a GNN-based approach that connects each node to its most similar neighbors during edge generation using Gumbel Softmax. As shown in Table 5, the similarity-

Method	Seegene			BreakHis		
	Ma-F1	Mi-F1	AUC	Ma-F1	Mi-F1	AUC
Dissim.	0.9708	0.9689	0.9973	0.9500	0.9286	0.9883
Rand.	0.9779	0.9767	0.9981	0.9500	0.9286	0.9825
<b>Sim.</b>	<b>0.9925</b>	<b>0.9922</b>	<b>0.9994</b>	<b>0.9730</b>	<b>0.9643</b>	<b>0.9942</b>

Table 5. Performance metrics of different edge generation methods (*Dissim.*: Dissimilarity, *Rand.*: Random Shuffle, *Sim.*: Similarity), with the best results are highlighted in **bold**.

based edges outperform random and dissimilarity-based methods across all evaluated metrics in both datasets. This demonstrates that using similarity-based edges effectively enhances contextual information.

## 6. Ablation study

### 6.1. Without vs. With Representative Images

Cluster	Seegene			BreakHis		
	Ma-F1	Mi-F1	AUC	Ma-F1	Mi-F1	AUC
w/o Rep.	0.9453	0.9455	0.9977	0.9500	0.9708	0.9286
<b>w/ Rep.</b>	<b>0.9925</b>	<b>0.9922</b>	<b>0.9994</b>	<b>0.9730</b>	<b>0.9643</b>	<b>0.9883</b>

Table 6. Performance metrics *without* (*w/o*) and *with* (*w/*) representative images on the Seegene and BreakHis datasets, with the best results are highlighted in **bold**.

The performance *without* using representative images is lower compared to *with* using representative images in both datasets, as shown in Table 6. This is because the model struggles to convey contextual information between diverse areas effectively. By selecting only the representative image for each area, the model can capture better contextual details, leading to improved interaction between diverse areas and thus enhancing overall performance. BreakHis shows a smaller difference between scenarios *without* and *with* representative images compared to the Seegene dataset (0.023

vs. 0.0472) as the number of redundant images is not as severe in BreakHis (Table 1). Conversely, in the Seegene dataset, performance is significantly improved when representative images are used as they capture essential contextual details among a high number of redundant images.

## 6.2. Representative Image Methods

Method	Seegene			BreakHis		
	Ma-F1	Mi-F1	AUC	Ma-F1	Mi-F1	AUC
Mean	0.9817	0.9988	0.9805	0.9258	0.9006	0.9446
Centroid	0.9876	0.9981	0.9867	0.9500	0.9649	0.9286
<b>Gumbel Softmax</b>	<b>0.9925</b>	<b>0.9922</b>	<b>0.9994</b>	<b>0.973</b>	<b>0.9643</b>	<b>0.9942</b>

Table 7. Performance metrics of different representative image methods (*Mean*, *Centroid*, and *Gumbel Softmax*) on the Seegene and BreakHis datasets, with the best results are highlighted in **bold**.

This study compares the performance of the *Mean*, *Centroid*, and *Gumbel Softmax* (*MicroMIL*) methods for selecting representative images. The *Mean* method averages all the image features in each cluster. The *Centroid* method selects the centroid of each cluster optimized by the DCE model. Lastly, the *Gumbel Softmax* method selects the image with the highest attention weight within the cluster. As shown in Table 7, performance is lowest with the *Mean* method, followed by the *Centroid*, and highest with *Gumbel Softmax* Method. This indicates that methods which consider the importance of individual images, like *Gumbel Softmax*, better capture the essential features of each cluster, leading to improved performance.

## 6.3. Representative Image Clusters

Cluster	Seegene			BreakHis		
	Ma-F1	Mi-F1	AUC	Ma-F1	Mi-F1	AUC
9	0.9150	0.9830	0.9962	0.9730	0.9643	0.9649
16	0.9810	0.9805	0.9986	<b>0.9730</b>	<b>0.9643</b>	<b>0.9883</b>
25	0.9612	0.9611	0.9982	0.9444	0.9286	0.9942
36	<b>0.9925</b>	<b>0.9922</b>	<b>0.9994</b>	0.9444	0.9286	0.9942
49	0.9675	0.9650	0.9971	0.9500	0.8929	0.9825

Table 8. Performance metrics across varying numbers of representative image clusters using deep cluster embedding (DCE) on the Seegene and BreakHis datasets, with the best results are highlighted in **bold**.

Table 8 presents the effect of varying the number of representative image clusters in both datasets. For the Seegene dataset, with an average of 150 redundant images per patient, the best performance is achieved with 36 clusters. In contrast, BreakHis, which has fewer redundant images, achieves optimal performance with 16 clusters, suggesting a need for more representative images as the number of redundant images increases.

## 6.4. Graph Layers Effect

Method	# of Graph Layers				
	0	1	2	3	4
Rand.	<b>0.9706</b>	0.9851	0.9779	0.9738	<b>0.9738</b>
Sim.	<b>0.9706</b>	<b>0.9889</b>	<b>0.9925</b>	<b>0.9740</b>	<b>0.9738</b>

Table 9. Comparison of Macro-F1 performance (*Rand.:* *Random Shuffling*, *Sim.:* *Similarity*) with varying number of graph layers. Fewer layers effectively consider adjacent images and achieve higher performance with Similarity. The best results are highlighted in **bold**.

The effects of graph edge generation under different number of graph layers is shown in Table 9. The result indicate that there is no difference in performance between *Random Shuffling* and *Similarity* (*MicroMIL*) when no layers are used, likely due to the lack of interaction with other images. Additionally, when many layers are used, the performance difference is negligible as it incorporates not only adjacent representative images but also most of the images. With a small number of layers, consideration is limited to adjacent representative images, leading to relatively high performance especially when using the *Similarity* method for edge generation.

## 7. Conclusion

We present *MicroMIL*, a weakly-supervised MIL framework that specifically designed for the unique characteristics of microscopy image analysis, particularly addressing the issues of unknown absolute positions and redundant images. By employing deep cluster embedding (DCE) to dynamically cluster images, using *Gumbel Softmax* to select representative images, and integrating a graph neural network (GNN) to model relationships between images, *MicroMIL* effectively captures both local and global contextual information. Validated on both real-world colon cancer data and the public BreakHis microscope dataset, *MicroMIL* outperforms existing MIL models. Our results demonstrate that *MicroMIL* significantly improves patient diagnostic accuracy and efficiency using microscopy images, setting a new standard in the field.

## Supplementary Material

### A. Private (Real-World) Dataset Description

We utilized a dataset obtained from the Seegene-Medical Foundation, which was approved by both the foundation’s institutional review board (SMF-IRB-2020-007)) and the collaborating partner university’s institutional review board (KAIST-IRB-23-214). This dataset comprises colorectal tissue images of 899 patients treated for colorectal cancer between 2021 and 2023. It was split by imaging dates, with post-November 2023 data designated as the test set. The



training set consists of 272 malignant and 330 normal cases, while the test set comprises 134 malignant and 123 normal cases. Overall, the dataset includes 82,761 malignant and 52,339 normal images.

The data was collected by Seegene-Medical Foundation, which has one of the largest diagnosis centers in the country. After collection, the tissue samples are fixed in 10% formalin and delivered to the pathology lab within 12 to 24 hours. The tissues are embedded in paraffin blocks, sectioned at approximately 3 micrometers ( $\mu\text{m}$ ) by clinical pathologists, and mounted on glass slides. Subsequently, the paraffin is removed, and the slides are stained with hematoxylin-eosin (H&E) before being covered with a cover glass for examination by the pathologists primarily at 40x and 100x magnifications.

For this study, an Augmentiqs Optical Module was attached to the microscope used by a pathologist. Cases selected by the pathologist for review were reassessed, and the device was used to automatically capture images by changing the magnification and field of view of the slide on the microscope equipped with this module for image generation purposes.

## B. Baseline code

Table 10 shows the urls of the authors' implementations of the compared methods.

Table 10. The Baseline urls

Method	URL link to the code
ABMIL [ICML'18] [20]	<a href="https://github.com/utayao/Atten-Deep-MIL">https://github.com/utayao/Atten-Deep-MIL</a>
MS-DA-MIL [CVPR'20] [17]	<a href="https://github.com/takeuchi-lab/MS-DA-MIL-CNN">https://github.com/takeuchi-lab/MS-DA-MIL-CNN</a>
DSMIL [CVPR'21] [29]	<a href="https://github.com/binli123/dsmil-wsi">https://github.com/binli123/dsmil-wsi</a>
TransMIL [NeurIPS'21] [35]	<a href="https://github.com/szc19990412/TransMIL">https://github.com/szc19990412/TransMIL</a>
DTFD-MIL [CVPR'22] [44]	<a href="https://github.com/hrzhang1123/DTFD-MIL">https://github.com/hrzhang1123/DTFD-MIL</a>

## References

- [1] S. Alkassar, B. A. Jebur, M. A. Abdullah, J. H. Al-Khalidy, and J. A. Chambers. Going deeper: a magnification-invariant approach for breast cancer classification using histopathological images. *IET Computer Vision*, 15(2):151–164, 2021. 2
- [2] D. Bardou, K. Zhang, and S. M. Ahmad. Classification of breast cancer based on histology images using convolutional neural networks. *IEEE Access*, 6:24680–24693, 2018. 1
- [3] Andrew H Beck, Ankur R Sangoi, Samuel Leung, Robert J Marinelli, Torsten O Nielsen, Marc J Van De Vijver, Robert B West, Matt Van De Rijn, and Daphne Koller. Systematic analysis of breast cancer morphology uncovers stromal features associated with survival. *Science translational medicine*, 3(108):108ra113–108ra113, 2011. 3
- [4] Y. Benhammou, B. Achchab, F. Herrera, and S. Tabik. Breakhis based breast cancer automatic diagnosis using deep learning: Taxonomy, survey, and insights. *Neurocomputing*, 375:9–24, 2020. 1, 2, 3, 6
- [5] Gianpaolo Bontempo, Nicola Bartolini, Marta Lovino, Federico Bolelli, Anni Virtanen, and Elisa Ficarra. Enhancing pfi prediction with gds-mil: A graph-based dual stream mil approach. In *International Conference on Image Analysis and Processing*, pages 550–562. Springer, 2023. 2, 6
- [6] Joshua Butke, Tatjana Frick, Florian Roghmann, Samir F El-Mashtoly, Klaus Gerwert, and Axel Mosig. End-to-end multiple instance learning for whole-slide cytopathology of urothelial carcinoma. In *MICCAI Workshop on Computational Pathology*, pages 57–68. PMLR, 2021. 4
- [7] D. Cai, X. Sun, N. Zhou, X. Han, and J. Yao. Efficient mitosis detection in breast cancer histology images by rcnn. In *2019 IEEE 16th International Symposium on Biomedical Imaging (ISBI 2019)*, pages 919–922. IEEE, 2019. 1
- [8] Tsai Hor Chan, Fernando Julio Cendra, Lan Ma, Guosheng Yin, and Lequan Yu. Histopathology whole slide image analysis with heterogeneous graph representation learning. In *Proceedings of the IEEE/CVF Conference on Computer Vision and Pattern Recognition*, pages 15661–15670, 2023. 1, 2, 6
- [9] Nicolas Coudray, Paolo Santiago Ocampo, Theodore Sakellaropoulos, Navneet Narula, Matija Snuderl, David Fenyő, Andre L Moreira, Narges Razavian, and Aristotelis Tsirigos. Classification and mutation prediction from non-small cell lung cancer histopathology images using deep learning. *Nature medicine*, 24(10):1559–1567, 2018. 1
- [10] A. J. Evans, E. A. Krupinski, R. S. Weinstein, and L. Pantanowitz. 2014 american telemedicine association clinical guidelines for telepathology: Another important step in support of increased adoption of telepathology for patient care. *Journal of Pathology Informatics*, 6, 2015. 2
- [11] Paweł Filipczuk, Thomas Fevens, Adam Krzyżak, and Roman Monczak. Computer-aided breast cancer diagnosis based on the analysis of cytological images of fine needle biopsies. *IEEE transactions on medical imaging*, 32(12):2169–2178, 2013. 3
- [12] Michael Gadermayr and Maximilian Tschuchnig. Multiple instance learning for digital pathology: A review of the state-of-the-art, limitations & future potential. *Computerized Medical Imaging and Graphics*, page 102337, 2024. 1, 4
- [13] Z. Gandomkar, P. C. Brennan, and C. Mello-Thoms. Modern: Multi-category classification of breast hikumartopathological image using deep residual networks. *Artificial intelligence in medicine*, 88:14–24, 2018. 2
- [14] M. Garcia-Rojo, D. De Mena, P. Muriel-Cueto, L. Atienza-Cuevas, M. Dominguez-Gomez, and G. Bueno. New european union regulations related to whole slide image scanners and image analysis software. *Journal of pathology informatics*, 10(1):2, 2019. 2
- [15] V. Gupta and A. Bhavsar. Breast cancer histopathological image classification: is magnification important? In *Proceedings of the IEEE conference on computer vision and pattern recognition workshops*, pages 17–24, 2017. 1, 2
- [16] Z. Han, B. Wei, Y. Zheng, Y. Yin, K. Li, and S. Li. Breast cancer multi-classification from histopathological images with structured deep learning model. *Scientific reports*, 7(1):4172, 2017. 3

- [17] Noriaki Hashimoto, Daisuke Fukushima, Ryoichi Koga, Yusuke Takagi, Kaho Ko, Kei Kohno, Masato Nakaguro, Shigeo Nakamura, Hidekata Hontani, and Ichiro Takeuchi. Multi-scale domain-adversarial multiple-instance cnn for cancer subtype classification with unannotated histopathological images, 2020. [2](#), [6](#), [7](#), [9](#)
- [18] Wentai Hou, Lequan Yu, Chengxuan Lin, Helong Huang, Rongshan Yu, Jing Qin, and Liansheng Wang.  $H^2$ -mil: exploring hierarchical representation with heterogeneous multiple instance learning for whole slide image analysis. In *Proceedings of the AAAI conference on artificial intelligence*, volume 36, pages 933–941, 2022. [1](#), [2](#), [6](#)
- [19] Peihao Huang, Yan Huang, Wei Wang, and Liang Wang. Deep embedding network for clustering. In *2014 22nd International conference on pattern recognition*, pages 1532–1537. IEEE, 2014. [2](#)
- [20] Maximilian Ilse, Jakub Tomczak, and Max Welling. Attention-based deep multiple instance learning. In *International conference on machine learning*, pages 2127–2136. PMLR, 2018. [1](#), [2](#), [6](#), [7](#), [9](#)
- [21] J. N. Iyengar. Whole slide imaging: The futurescape of histopathology. *Indian Journal of Pathology and Microbiology*, 64(1):8, 2021. [2](#)
- [22] Eric Jang, Shixiang Gu, and Ben Poole. Categorical reparameterization with gumbel-softmax. *arXiv preprint arXiv:1611.01144*, 2016. [2](#), [4](#)
- [23] Diederik P Kingma and Jimmy Ba. Adam: A method for stochastic optimization. *arXiv preprint arXiv:1412.6980*, 2014. [6](#)
- [24] Andrei V. Konstantinov and Lev V. Utkin. Multi-attention multiple instance learning, 2021. [2](#)
- [25] Marek Kowal, Paweł Filipczuk, Andrzej Obuchowicz, Józef Korbicz, and Roman Monczak. Computer-aided diagnosis of breast cancer based on fine needle biopsy microscopic images. *Computers in biology and medicine*, 43(10):1563–1572, 2013. [3](#)
- [26] N. Kumar, R. Gupta, and S. Gupta. Whole slide imaging (wsi) in pathology: current perspectives and future directions. *Journal of digital imaging*, 33(4):1034–1040, 2020. [2](#)
- [27] Han Le, Rajarsi Gupta, Le Hou, Shahira Abousamra, Danielle Fassler, Luke Torre-Healy, Richard A Moffitt, Tahsin Kurc, Dimitris Samaras, Rebecca Batiste, et al. Utilizing automated breast cancer detection to identify spatial distributions of tumor-infiltrating lymphocytes in invasive breast cancer. *The American journal of pathology*, 190(7):1491–1504, 2020. [1](#)
- [28] Y. Lee, J. H. Park, S. Oh, K. Shin, J. Sun, M. Jung, ..., and S. Kwon. Derivation of prognostic contextual histopathological features from whole-slide images of tumours via graph deep learning. *Nature Biomedical Engineering*, pages 1–15, 2022. [1](#)
- [29] Bin Li, Yin Li, and Kevin W. Eliceiri. Dual-stream multiple instance learning network for whole slide image classification with self-supervised contrastive learning, 2021. [2](#), [6](#), [7](#), [9](#)
- [30] Vinod Nair and Geoffrey E Hinton. Rectified linear units improve restricted boltzmann machines. In *Proceedings of the 27th international conference on machine learning (ICML-10)*, pages 807–814, 2010. [5](#)
- [31] H. G. Nguyen, A. Blank, H. E. Dawson, A. Lugli, and I. Zlobec. Classification of colorectal tissue images from high throughput tissue microarrays by ensemble deep learning methods. *Scientific reports*, 11(1):1–11, 2021. [2](#)
- [32] Anabik Pal, Zhiyun Xue, Kanan Desai, Adekunbiola Aina F Banjo, Clement Akinfolarin Adepiti, L Rodney Long, Mark Schiffman, and Sameer Antani. Deep multiple-instance learning for abnormal cell detection in cervical histopathology images. *Computers in Biology and Medicine*, 138:104890, 2021. [3](#)
- [33] Ramprasaath R Selvaraju, Michael Cogswell, Abhishek Das, Ramakrishna Vedantam, Devi Parikh, and Dhruv Batra. Grad-cam: Visual explanations from deep networks via gradient-based localization. In *Proceedings of the IEEE international conference on computer vision*, pages 618–626, 2017. [2](#)
- [34] M. Shaban, R. Awan, M. M. Fraz, A. Azam, Y. W. Tsang, D. Snead, and N. M. Rajpoot. Context-aware convolutional neural network for grading of colorectal cancer histology images. *IEEE transactions on medical imaging*, 39(7):2395–2405, 2020. [1](#)
- [35] Zhuchen Shao, Hao Bian, Yang Chen, Yifeng Wang, Jian Zhang, Xiangyang Ji, and Yongbing Zhang. Transmil: Transformer based correlated multiple instance learning for whole slide image classification, 2021. [1](#), [2](#), [6](#), [7](#), [9](#)
- [36] F. A. Spanhol, L. S. Oliveira, C. Petitjean, and L. Heutte. Breast cancer histopathological image classification using convolutional neural networks. In *2016 international joint conference on neural networks (IJCNN)*, pages 2560–2567, 2016. [2](#)
- [37] Yi Sun, Xiaogang Wang, and Xiaoou Tang. Deeply learned face representations are sparse, selective, and robust. In *Proceedings of the IEEE conference on computer vision and pattern recognition*, pages 2892–2900, 2015. [5](#)
- [38] L. A. Torre, R. L. Siegel, E. M. Ward, and A. Jemal. Global cancer incidence and mortality rates and trends—an update—global cancer rates and trends—an update. *Cancer epidemiology, biomarkers & prevention*, 25(1):16–27, 2016. [1](#)
- [39] Jerry Wei, Arief Suriawinata, Bing Ren, Xiaoying Liu, Mikhail Lisovsky, Louis Vaickus, Charles Brown, Michael Baker, Naofumi Tomita, Lorenzo Torresani, et al. A petri dish for histopathology image analysis. In *Artificial Intelligence in Medicine: 19th International Conference on Artificial Intelligence in Medicine, AIME 2021, Virtual Event, June 15–18, 2021, Proceedings*, pages 11–24. Springer, 2021. [3](#)
- [40] Junyuan Xie, Ross Girshick, and Ali Farhadi. Unsupervised deep embedding for clustering analysis. In *International conference on machine learning*, pages 478–487. PMLR, 2016. [4](#)
- [41] Conghao Xiong, Hao Chen, Joseph J.Y. Sung, and Irwin King. Diagnose like a pathologist: Transformer-enabled hierarchical attention-guided multiple instance learning for whole slide image classification. In Edith Elkind, editor, *Proceedings of the Thirty-Second International Joint Conference on Artificial Intelligence, IJCAI-23*, pages 1587–1595.

International Joint Conferences on Artificial Intelligence Organization, 8 2023. Main Track. [2](#)

- [42] R. Yan, F. Ren, Z. Wang, L. Wang, T. Zhang, Y. Liu, ..., and F. Zhang. Breast cancer histopathological image classification using a hybrid deep neural network. *Methods*, 173:52–60, 2020. [1](#)
- [43] Yang Yang, Yanlun Tu, Houchao Lei, and Wei Long. Hamil: Hierarchical aggregation-based multi-instance learning for microscopy image classification. *Pattern Recognition*, 136:109245, 2023. [3](#)
- [44] Hongrun Zhang, Yanda Meng, Yitian Zhao, Yihong Qiao, Xiaoyun Yang, Sarah E. Coupland, and Yalin Zheng. Dtfmil: Double-tier feature distillation multiple instance learning for histopathology whole slide image classification, 2022. [1](#), [2](#), [6](#), [7](#), [9](#)